

Multi-Agent Relative Pose Estimation with UWB and Constrained Communications

Andrew Fishberg

Jonathan P. How

Abstract—Inter-agent relative localization is critical for any multi-robot system operating in the absence of external positioning infrastructure or prior environmental knowledge. We propose a novel inter-agent relative 2D pose estimation system where each participating agent is equipped with several ultra-wideband (UWB) ranging tags. Prior work typically supplements noisy UWB range measurements with additional continuously transmitted data, such as odometry, making these approaches scale poorly with increased swarm size or decreased communication throughput. This approach addresses these concerns by using only locally collected UWB measurements with no additionally transmitted data. By modeling observed ranging biases and systematic antenna obstructions in our proposed optimization solution, our experimental results demonstrate an improved mean position error (while remaining competitive in other metrics) over a similar state-of-the-art approach that additionally relies on continuously transmitted odometry.

I. INTRODUCTION

Multi-robot approaches improve the efficiency and robustness of large-scale decentralized tasks such as search & rescue [1], warehouse automation [2], and planetary exploration [3]. To operate and divide tasks effectively, all these systems require an understanding of where agents and their peers are within a common reference frame. In practice this is often achieved by localizing within an a priori map or using an external measurement system like GPS or motion capture (mocap). In scenarios where these convenient technologies are unavailable or infeasible, common approaches utilize both relative localization [4] and decentralized SLAM [5]–[7] techniques.

Relative localization is often computed from a set of relative range or relative angle measurements. In turn, these inputs are estimated by measuring a received signal’s time of arrival (TOA), time difference of arrival (TDOA), angle of arrival (AOA), or received signal strength (RSS) [8]. Furthermore, said signals have many possible forms: acoustic [9], Bluetooth Low Energy (BLE) [10], Radio Frequency Identification (RFID) [11], or WiFi [12], [13]. Within the last decade, ultra wideband (UWB) has matured into a reliable, inexpensive, and commercially available RF solution for data transmission, TOA or TDOA ranging, and localization. As a result, many roboticists have already begun to incorporate UWB into their work (see Section II). Several advertised properties make UWB particularly noteworthy: precision of approximately 10 centimeters, ranges up to 100 meters, resilience to multipath, no dependency on line of sight

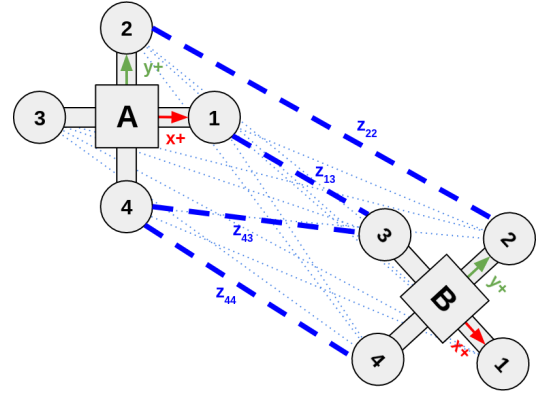


Fig. 1: Diagram of two agents, RobotA and RobotB, each with their respective relative coordinate frames and UWB sensors labeled. Relative range measurements are shown between each pair of inter-agent antennas in blue (N.B.: the dashed and dotted blue lines are only differentiated for the sake of visual clarity, they represent the same type of measurements). These 16 unique measurements are denoted as z_{ij} where i and j are the corresponding antenna indices for RobotA and RobotB respectively.

(LOS), low power consumption, and 100 Mbit/s communication speeds [14]. Nevertheless, UWB measurements are not immune from ranging errors or noise, the modeling and correction of which is an active research topic within the robotics community [15]–[18]. A common approach among UWB relative localization work supplements noisy UWB ranging measurements with additional continuously transmitted data, such as odometry [19] and visual inter-agent tracks [20], [21]. While this additional data improves overall estimation accuracy, its transmission causes poor scalability with respect to increased swarm size or decreased communication throughput.

This paper presents a multi-tag UWB relative 2D pose estimation system built for future integration into a larger resource-aware distributed SLAM pipeline. Specifically, our system aims to produce collaborative inter-agent loop-closures (i.e. relative pose estimates between agents) at a higher rate than visual loop-closure techniques utilized by decentralized visual SLAM systems [5], but with a lower communication footprint and absolute accuracy. We achieve this by equipping each agent with multiple UWB tags in a known prior configuration (such as shown in Figure 1), allowing our system to produce full relative pose estimates between agents using only locally collected UWB measurements (i.e. no inter-agent data, such as odometry, is exchanged). By using only local measurements, the host distributed SLAM system can allocate its full limited bandwidth to the transmission

* Work supported in part by DOE, NNSA, and ALB funding. Both authors are with the MIT Department of Aeronautics and Astronautics. Contact at {fishberg, jhow}@mit.edu

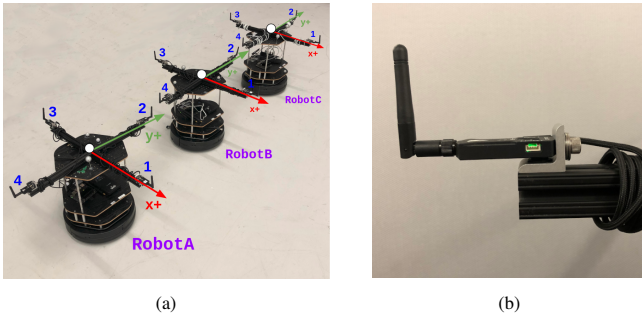


Fig. 2: (a) Photo of our experimental robots. Each is comprised of a Turtlebot2 base, a Jetson Nano, and four Nooploop UWB sensors. Robots are manually controlled with a wireless Logitech Gamepad. (b) A close up showing how UWB sensors are attached radially from the aluminum mounting bracket. This is done to ensure antenna clearance and to avoid direct contact with metal.

and detection of the higher fidelity visual loop-closures.¹

Our approach is distinguished from similar UWB-enabled relative localization works by completely forgoing the use of transmitted (remote) measurements, effectively trading off a small reduction in absolute estimation accuracy for a superior (i.e., eliminated) communication footprint and thus scalability. Despite this potential performance sacrifice, by accounting for the measurement errors (i.e., systemic UWB ranging biases and systematic obstructions) in the optimization process, we achieve superior mean position accuracy and comparable performance on other metrics to prior work [19] without the need to continuously transmit odometry estimates.

This paper’s contributions are: (1) An in-depth analysis and modeling of the observed noise characteristics of UWB ranging measurements (Section III); (2) A customized solution for UWB-based relative localization that takes into account the specific observed noise properties, formulated as a nonlinear least squares (NLLS) optimization (Section IV); and (3) Experimental results that demonstrate the merits of the developed solution (Section V).

II. RELATED WORK

The recent paper [23] provides an excellent overview recent UWB usage in robotics and IoT pipelines. When considering UWB for mobile robotics, the work naturally separates into several categories.

Known anchor points: In these systems a target with a single UWB tag is trilaterated by several UWB anchor points at known global locations. These approaches are conceptually similar to GPS where each range measurement is coming from a satellite with a known absolute position, although anchors are often assumed to be static. Since the target has a single tag, the target’s orientation is not observable from just UWB measurements. Works using these assumptions

¹As the resource-aware detection of collaborative loop-closures is a research topic in itself [22], how the host decentralized SLAM pipeline can best utilize these UWB loop-closures remains a subject for future work. Promising potential directions include: (1) to improve the state estimation in the absence of visual loop-closures and (2) to inform the priority of transmitting potential loop-closure between agents.

produce improved state estimation results by fusing the global UWB position estimation with some combination of dynamics models, odometry (e.g. wheel odometry or visual odometry), and IMU data [24]–[28].

Static features: These works assume there are one or more static UWB anchors with not necessarily known positions. The observed anchor(s) are treated like static SLAM feature(s) and fused with odometry data to perform localization [12], [29], [30]. This is also comparable to [13], but WiFi hotspot relative bearing measurements are used instead of UWB ranging measurements. Also in this category is [3], [31], where the robot deploys a stationary UWB node during exploration, effectively marking a static point in the environment useful for future loop-closure detection.

Observability results: Mobile agents, each equipped with one (or possibly two in the case of [32]) ranging tags, take several temporally spaced relative range measurements while each traversing some trajectory. Agents track their local trajectory through odometry or IMU dead reckoning and share it with other agents. As shown in [4], [33], if the trajectories have sufficient relative motion then the relative pose between agents can be recovered.

Multi-tag pose estimation: Mobile agents are each equipped with multiple non-collocated tags at known relative positions on the agent. With sufficient tags, relative position and orientation can be observed with UWB measurements alone [34]–[36]. Furthermore, additional measurements, such as odometry, optical flow, IMU readings, and altitude measurements can be communicated between agents and fused with the UWB measurements in [19] and [37] to improve results and achieve observability respectively. Ref. [19] presents similar work to this paper, but it differs in the particle filtering approach and by the need to continuously share odometry between agents which contrasts with the objectives of this work. The similarities between the hardware setup and experiments allow for a useful baseline of comparison for our experimental results (see Section V-E).

Correcting UWB ranging errors: Works in this category model the ranging errors or design calibration schemes to correct errors [15]–[18]. Additionally, as many of the commercially available UWB sensors provide ranging measurements as a black box, certain algorithmic choices and calibration parameters are hidden from the user.

Full pipelines: Omni-swarm [21] (and earlier work [20], [38]) is perhaps the most complete and comprehensive UWB localization system. However, the impressive results achieved by the system heavily rely on omni-directional cameras for tracking neighboring agents and, although decentralized, mandates a continuous exchange of odometry and other measurements between all agents. Additionally, [39] provides an interesting full pipeline approach, but has each agent’s role alternate between active swarm member and static anchor node.

III. CHARACTERIZING UWB NOISE

A. Robot and UWB Setup

All experiments were conducted with a set of robots (see Figure 2a) each equipped with a Turtlebot2 base, NVIDIA Jetson Nano, and four Nooploop UWB sensors. UWB sensors are positioned $R = 0.35$ m from the center of the robot to the upright UWB antenna.² The mounting bracket is made of aluminum and UWB modules are mounted radially for antenna clearance (see Figure 2b).

In accordance to the LinkTrack manual [40], all antennas are all positioned upright, since their xy -plane has better omni-directivity than their z -axis. UWB nodes are numbered as in Figure 1. Nodes are configured into *Distributed Ranging (DR) Mode*, to enable measuring relative range without the need for stationary anchors, and configured to use Channel 3 (3,744-4,243.2 MHz) [41]. All tests were performed in a motion capture space for high-precision ground truth pose.

The Nooploop LinkTrack P was selected over other considered products, such as the Pozyx Developer Tag or DWM1001 Development Board, because: (1) the LinkTrack P has a slim form factor (5.5cm x 3cm x 0.75cm), light weight (33g), and easy mounting via a 1/4-20 screw hole; (2) Nooploop provides an out of the box ROS driver; and (3) in our trials using 8 tags, the LinkTrack P provided measurements at steady 50Hz, while the Pozyx Developer Tag fluctuated around 5Hz.

B. Range Measurement Bias & Noise

Experiments were performed to characterize the UWB ranging noise. Figure 3a shows a sample of measurement error between two stationary UWB nodes with direct line-of-sight (LOS), as shown in Figure 3c. Three important observations are: (1) Contrary to the common measurement noise assumption, the error appears neither zero mean nor Gaussian (i.e. shown sample fails the `scipy.stats.normaltest` function [42], an implementation of the D’Agostino and Pearson’s normal test [43], with a p -value of 2.36×10^{-6}). (2) Sensors tend to consistently over-estimate the relative distance between nodes. (3) Within our operating environment, the mean error between a pair of unobstructed UWB nodes remains approximately constant independent of distance between nodes or when data was collected. Additional evidence of this claim can be seen in unobstructed portions of Figures 4b-4e, a follow-on experiment motivated in Section III-C.

C. Antenna Obstruction & Interference

Since UWB relative range measurements are a TOA measuring scheme, any delays on receiving a signal (i.e. propagating through an obstruction) will result in a ranging over-estimation. This helps make sense of the substantial 41 cm increase of mean error shown in Figures 3b and 3d when

²As the robustness and accuracy of the estimated pose computed from trilateration is positively correlated with the length of the sensor baseline the R separation was selected to closely resemble the arm length of a medium-sized quadrotor, in anticipation for future work, as well as allowing for a fair comparison to the results of [19], who tested a similar baseline.

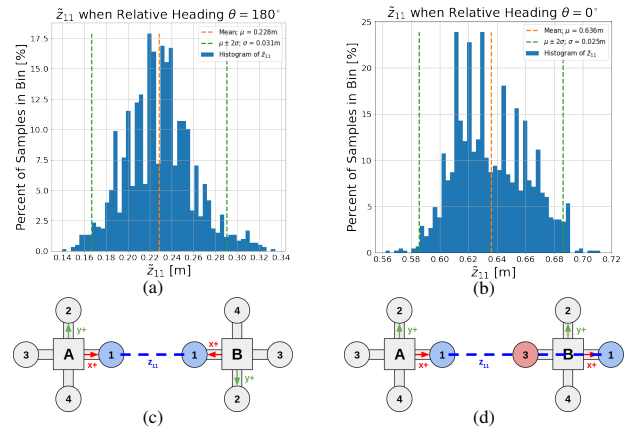


Fig. 3: Histograms showing the measurement error for two separate data collects of \tilde{z}_{11} (50Hz for 30 s). Measurement error \tilde{z}_{11} is the difference between the UWB range measurement and ground truth distance as measured by a Vicon system. Histogram (a)/(b) correspond to the error from the direct line-of-sight/obstructed configuration shown in (c)/(d) respectively. Neither of these distributions would be well-modeled as Gaussian. The orange lines and green lines show the calculated sample mean and \pm two standard deviation boundaries respectively. With no obstruction, we see an average of 23 cm over-estimation of z_{11} , and when obstructed, this increases by 41 cm, to an average of 64 cm over-estimation. Thus the error is not zero mean (and the mean increases further when obstructed).

compared to Figures 3a and 3c. Furthermore, the LinkTrack P manual [40] offers several notes regarding obstruction: (1) Signal can propagate through 2 or 3 solid walls, but each wall introduces approximately 30 cm of error and a decreased maximum ranging distance. (2) The distance between each node and the obstruction affects ranging accuracy; the best results occur when the obstruction is equally spaced between the antennas, the worst results occur when the obstruction is close to one of the antennas. This presents a noteworthy concern: as agents move relative to each other, fixed obstructions on the robot, such as a third antenna, can pass between the ranging pair causing an obstructed measurement. This obstruction is worsened by its guaranteed proximity to at least one of the ranging antennas. This eclipse-like effect can be observed in Figures 4b-4e, where clear over-estimation error spikes occur predictably at specific relative heading for each pair of antennas.

While it is difficult to pinpoint the exact cause of this obstruction, it appears to be a combination of proximity to other antennas, metal, and other components. Though it would be possible to mount these sensors in a different configuration to mitigate this, in reality there are times when obstructions cannot be avoided, especially as one begins to consider quadrotors and 3D environments. Thus, we will treat this interference as part of the given hardware setup which in turn must be mitigated algorithmically.³

³Inspection of the received RSSI does not appear to provide any meaningful way to detect the current obstruction. As per [40], when RSSI is less than 6 dB, it is likely to be in the line-of-sight state, and when greater than 10 dB, it is likely to be in the non-line-of-sight or multipath state. Despite this, we consistently observe `fp_rssi` and `rx_rssi` of approximately -81.0 dB and -78.0 dB respectively, with a 0.5 dB minimum resolution.

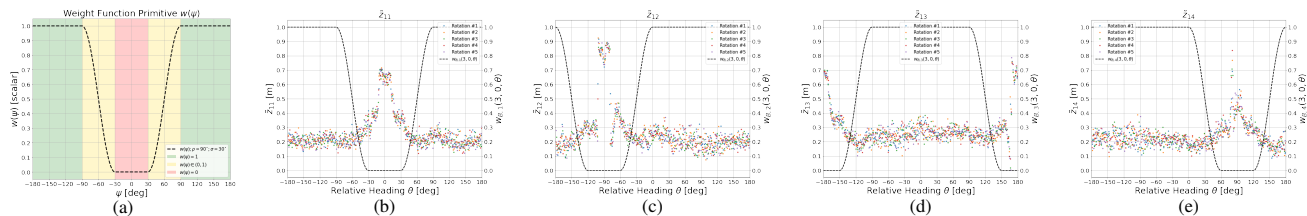


Fig. 4: (a) Weight function primitive $w(\psi)$ with parameters $\sigma = 30^\circ$ and $\rho = 90^\circ$ (see Eq. 4). Colors represent the segments of the piecewise function, and align with the colors in the Figure 5. (b-d) Plots of \tilde{z}_{11} through \tilde{z}_{14} with respect to R_B 's relative heading. Shown data is all from the same data collection where R_A was kept stationary while R_B performed 5 in place counter-clockwise revolutions at approximately 60 deg/s. Each revolution is denoted in a different color to highlight this noise pattern is repeatable. The overlaid weight function $w_{B,j}(\mathbf{x})$ (see Eq. 7) shows that areas with error spikes correspond to relative headings correctly predicted and devalued by $w_{B,j}(\mathbf{x})$. Additionally, when the error is not spiking, we see additional evidence that the noise is not zero mean, as discussed in Section III-B.

IV. OPTIMIZATION FORMULATION

Consider two robots, *RobotA* and *RobotB*, denoted as R_A and R_B respectively. Labels are assigned such that R_A is trying to estimate R_B 's relative pose with respect to R_A 's reference frame. Let R_B 's relative pose be described by the state vector \mathbf{x} . Each robot has N UWB range sensors, uniquely identified with an integer index from the set $S := \{1, \dots, N\}$. Assuming R_A and R_B have the same antenna layout, the relative position vector of the k th antenna of a robot with a pose vector of \mathbf{T} is defined as $\alpha_k(\mathbf{T})$. Since we are in R_A 's reference frame, $\alpha_i(\mathbf{0})$ gives the position vector of R_A 's i th antenna, while $\alpha_j(\mathbf{x})$ gives the position vector of R_B 's j th antenna. Thus, let d_{ij} be the distance between R_A 's i th antenna and R_B 's j th antenna when R_B is at \mathbf{x} , such that:

$$d_{ij}(\mathbf{x}) = \|\alpha_i(\mathbf{0}) - \alpha_j(\mathbf{x})\|_2 \quad (1)$$

For each discrete timestep t , N^2 raw relative range measurements are taken, one per unique pair of R_A and R_B antennas. These measurements are denoted as $z_{ij}^{(t)}$ where i is R_A 's i th antenna, j is R_B 's j th antenna, and t is the given discrete timestep. Note that as long as we use only our locally collected $z_{ij}^{(t)}$ measurements, we will not require any additional information be exchanged between agents.

A. Calibrated Range Measurements

As noted in Section III-B, raw UWB relative range measurements $z_{ij}^{(t)}$ are subject to biases between pairs of antennas μ_{ij} as well as general non-Gaussian noise. Thus, we can improve quality and robustness of our UWB relative range measurement by: (1) Performing a one-time calibration process to measure the consistent measurement bias μ_{ij} between nodes i and j respectively (implementation discussed in Section V-B). (2) Smoothing sequential UWB relative range measurements with a simple moving average filter, which should make the signal more closely track the mean while introducing a slight signal delay.

Let $\hat{z}_{ij}^{(t)}$ be a calibrated relative range measurement,

$$\hat{z}_{ij}^{(t)} = -\mu_{ij} + \frac{1}{W} \sum_{k=0}^{W-1} z_{ij}^{(t-k)}. \quad (2)$$

Here we are effectively running a moving average filter over the W most recent z_{ij} range measurements and subtracting

out the mean bias μ_{ij} . The choice of W can be selected to trade-off between noise robustness and signal delay, but choosing it to be too large will make rapid relative yaw maneuvers unobservable (i.e., an in-place 360° spin within a single W period would appear as if the sensor did not move).

B. 2D Formulation - Simple Trilateration on (x, y, θ)

Let R_A and R_B be operating in 2D space, making R_B 's relative pose be described as $\mathbf{x} = [x, y, \theta]^T$, where x, y, θ are the relative x -coordinate, y -coordinate, and heading (yaw) respectively. Let each robot be equipped with $N \geq 3$ UWB relative range sensors and have their antenna arranged in a non-degenerate layout. Consider the nonlinear least square (NLLS) trilateration pose estimation problem:

$$\operatorname{argmin}_{\mathbf{x}} \sum_{i \in S} \sum_{j \in S} \left(d_{ij}(\mathbf{x}) - \hat{z}_{ij}^{(t)} \right)^2 \quad (3)$$

This formulation can be thought of as our baseline implementation that will be augmented in Section IV-C.

C. 2D Formulation - Antenna Weighting

As noted in Section III-C, antennas provide unreliable range measurements when obstructed by another antenna. Since these obstructions are reliably predictable given a specific hardware layout and state, we want to devalue NLLS terms involving an obstructed antenna. This approach is preferable since we are encoding our a priori system knowledge directly into our optimization problem, while more general techniques, such as the use of a Huber loss function, rely on rejecting data based on general outlier criteria. Our approach can be thought of as an analogue to a Maximum Likelihood Estimator formulation where a measurement covariance matrix is specified as a function of state.

Consider the 2π periodic weight function $w(\psi)$, specified here on the angular interval $\psi \in [-\pi, \pi]$, and shown plotted in Figure 4a:

$$w(\psi) = \begin{cases} 1 & \rho \leq |\psi| \leq \pi \\ \frac{1}{2} \cos\left(\frac{\pi(\psi+\rho)}{\rho-\sigma}\right) + \frac{1}{2} & -\rho < \psi < -\sigma \\ \frac{1}{2} \cos\left(\frac{\pi(\psi-\sigma)}{\rho-\sigma}\right) + \frac{1}{2} & \sigma < \psi < \rho \\ 0 & 0 \leq |\psi| \leq \sigma \end{cases} \quad (4)$$

where σ and ρ , related by $0 \leq \sigma \leq \rho \leq \pi$, are predefined constants defining the “stop-band” end angle and “pass-band” begin angle respectively. This function can be thought of as a piecewise step function with a smooth transition between high and low values, in the form of re-scaled and shifted cos segments. Compared to a standard step function, this weight function is differentiable, a useful property for optimization. This function will serve as a primitive for the more specialized weight functions developed in Eqs. 6, 7, and 8.

Although this overall formulation is agnostic to exact sensor numbers and layout, we will develop the remainder of this section using the experimental hardware setup described in Section III-A. Let our 2D robots have an antenna layout as shown in Figure 2a and described by the expression:

$$\alpha_k(\mathbf{T}) = \begin{bmatrix} x + R \cos(\frac{\pi}{2}(k-1) + \theta) \\ y + R \sin(\frac{\pi}{2}(k-1) + \theta) \end{bmatrix} \quad (5)$$

where relative pose T has relative components x, y, θ and $R = 0.35$ m.

Based on our hardware layout, consider the specialized weight functions $w_{A,i}(\mathbf{x})$ and $w_{B,j}(\mathbf{x})$ for discounting non-linear least squared terms involving R_A 's i th antenna and R_B 's j th antenna respectively:

$$w_{A,i}(\mathbf{x}) = w(\arctan(y, x) - \frac{\pi}{2}(i+1)) \quad (6)$$

$$w_{B,j}(\mathbf{x}) = w(\theta - \arctan(y, x) - \frac{\pi}{2}(j-1)) \quad (7)$$

Note that $w_{A,i}(\mathbf{x})$ and $w_{B,j}(\mathbf{x})$ are just phase shifted versions of $w(\psi)$ based on the components in $\mathbf{x} = [x, y, \theta]^T$. As shown in Figures 4b-4e, these weight functions are aligned so that they devalue measurements involving antennas on the “far” side of either robot. See Figure 5 for a visual example.

For convenience, we can then combine $w_{A,i}(\mathbf{x})$ and $w_{B,j}(\mathbf{x})$ into a single weighting $w_{ij}(\mathbf{x}) = w_{A,i}(\mathbf{x}) \cdot w_{B,j}(\mathbf{x})$. Augmenting Eq. 3 with this weighting yields

$$\underset{\mathbf{x}}{\operatorname{argmin}} \sum_{i \in \{1, \dots, N\}} \sum_{j \in \{1, \dots, N\}} w_{ij}(\mathbf{x}) \left(d_{ij}(\mathbf{x}) - \hat{z}_{ij}^{(t)} \right)^2. \quad (8)$$

When using the parameters $\sigma = 30^\circ$ and $\rho = 90^\circ$, this means that, at any given time, at most 7 of 16 measurements between a pair of robots can be ignored (i.e. four measurements coming from R_A 's ignored antenna, four measurements coming from R_B 's ignored antenna, with one measurement being ignored twice). Although with reliable measurements only three antennas per agent are needed to have a fully observable 2D system, the redundant fourth antenna allows us to entirely ignore the obstructed measurements within a given pair of agents while maintaining full 2D observability.

D. Optimization Initialization

When computationally solving the nonlinear problems in Eq. 3 or 8, the optimizer requires initial relative pose \mathbf{x}_0 . Although we cannot guarantee convexity on either equation, as sufficiently erroneous measurements $\hat{z}_{ij}^{(t)}$ can make either equation behave irregularly, typically we observe that optimizing Eq. 3 yields the same result regardless of selected

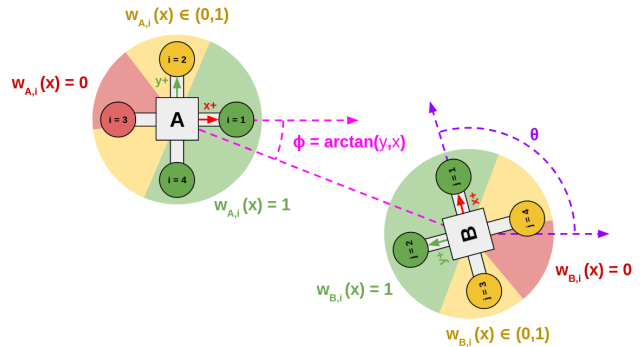


Fig. 5: Visualization of weighting functions $w_{A,i}(\mathbf{x})$ and $w_{B,i}(\mathbf{x})$ when $\mathbf{x} = [3, -1, 100^\circ]^T$. Here, the green, yellow, and red colors correspond to the colored weight segments of $w(\psi)$ in Figure 4a. In this scenario, optimization terms involving R_A 's $i = 3$ antenna are ignored, while terms involving R_A 's $i = 2$ antenna and/or R_B 's $j = 3$ or $j = 4$ antennas are devalued.

TABLE I: Comparison of Mean Difference Predicted Position (MDPP) and Mean Difference Predicted Absolute Heading (MDPAH) over 10000 trials for different optimization equations initialized with various \mathbf{x}_0 . Note that MDPP and MDPAH are indicative of how the optimization results differ between the selected initial conditions.

Opt. Eq.	Compared \mathbf{x}_0	MDPP [m]	MDPAH [deg]
Eq. 3	$\mathbf{0}$ vs \mathbf{x}_{gt}	0.002	0.067
Eq. 8	$\mathbf{0}$ vs \mathbf{x}_{gt}	1.109	41.704
Eq. 8	\mathbf{x}_{res} vs \mathbf{x}_{gt}	0.018	0.884

the \mathbf{x}_0 , while Eq. 8 very much depends on the selected \mathbf{x}_0 . To address this, in practice we perform a two staged optimization, i.e. we initialize Eq. 8 with \mathbf{x}_{res} , which is the result of solving Eq. 3 when initialized at $\mathbf{x}_0 = \mathbf{0}$.

To demonstrate the utility of this two-step process, a simulation was written in which ground truth state \mathbf{x}_{gt} was sampled from the uniform distribution $[\mathcal{U}_{[-5,5]}, \mathcal{U}_{[-5,5]}, \mathcal{U}_{[0,360]}]^T$ such that $\| [x, y]^T \|_2 \geq 1$ and z_{ij} was sampled by adding $\mathcal{N}(0, 0.2)$ to the ground truth distances. Table I shows the results after 10000 trials, which highlight that solving Eq. 3 effectively finds the same local minimum whether initialized with $\mathbf{0}$ or \mathbf{x}_{gt} , but Eq. 8 often finds the “wrong” local minimum if initialized with $\mathbf{0}$ and the “correct” local minimum if initialized with \mathbf{x}_{res} (i.e., the proposed two-step process).

V. EXPERIMENTAL RESULTS

A. Experimental Setup & Implementation

Experimental trials were conducted using the hardware in Section III-A and the algorithms in Section IV. All code was written using Python 3 and ROS [44]. Optimization was done using `scipy.optimize.minimize` with the `trust-constr` method [42]. Calibrated measurements $\hat{z}_{ij}^{(t)}$ are generated at 50Hz, the sensor operating rate, and sampled by the optimization code as needed. The optimization implementation runs in real-time at approximately 10Hz on an Intel i7-6700 with 8GB of RAM. This could easily be sped up by switching to a C++ implementation. Collected UWB data is post-processed with several alternative algorithms to compare results. When applicable, we use

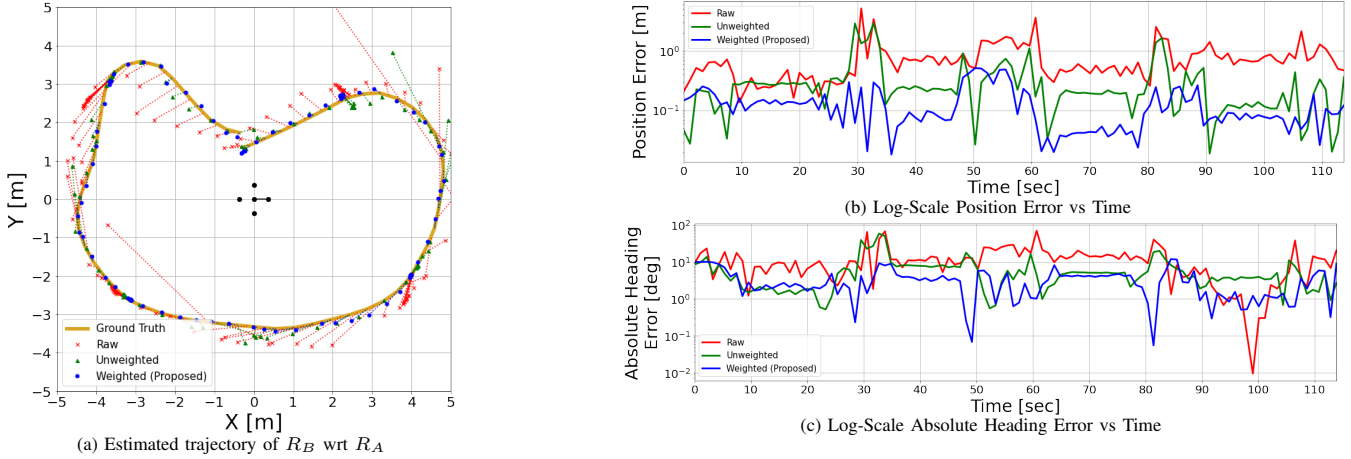


Fig. 6: Results from experimental trial where R_B is manually driven in a kidney bean shape while pausing briefly throughout the trajectory. To prevent visual clutter, only estimations from the Raw, Unweighted, and Weighted (Proposed) algorithms are shown alongside the mocap ground truth. Where applicable the parameters $\sigma = 30^\circ$, $\rho = 90^\circ$, and $W = 50$ (i.e. 1 sec of samples since measurements occur at 50Hz) are used. (a) Shows each algorithm’s predicted position estimate (at 1Hz) and draws an error line between each estimated point and its corresponding ground truth point. (b) Shows each algorithm’s log-scale positional error versus time for the given trial. (c) Similarly shows each algorithm’s log-scale absolute heading error for the given trial. Examining the plots (b) and (c), we see Weighted (Proposed) provides the best estimate of position and heading a vast majority of the times within the trajectory. See specific calculated mean, max, and standard deviation values, as well as all other results, in Tables II and III.

parameters $\sigma = 30^\circ$, $\rho = 90^\circ$, and $W = 50$ (measurements sampled at 50Hz). Specifically, these algorithms are:

- Raw: Optimizes Eq. 3, but uses the “raw” $z_{ij}^{(t)}$ measurement instead of the calibrated $\hat{z}_{ij}^{(t)}$.
- Shift only: Refers to Eq. 3, but uses the $z_{ij}^{(t)} - \mu_{ij}$ instead of the calibrated $\hat{z}_{ij}^{(t)}$.
- MovingAvg only: Refers to Eq. 3, but uses $\frac{1}{W} \sum_{k=0}^{W-1} z_{ij}^{(t-k)}$ instead of the calibrated $\hat{z}_{ij}^{(t)}$.
- Unweighted: Refers to Eq. 3 as written.
- Weighted (Proposed): Optimizes Eq. 8.

Comparing the results of Raw, Shift only, and MovingAvg only with Unweighted will clearly show the benefits of using the calibrated $\hat{z}_{ij}^{(t)}$. Similarly, comparing the results of Unweighted and Weighted shows the benefits of adding the NLLS weighting $w_{ij}(\mathbf{x})$.

B. Calibration

Calibration means μ_{ij} were found by placing R_A and R_B a known distance apart (3 m) and rotating R_B in place at approximately 60 deg/sec. After R_B completed a full revolution, R_A was rotated approximately 30° before R_B resumed rotating. The process took approximately 90 seconds and, afterwards, μ_{ij} values were calculated by averaging \hat{z}_{ij} while omitting regions of antenna obstructions spikes, similar to Figures 4b-4e. The following μ_{ij} values were computed:

$$\begin{aligned}
 \mu_{11} &= 0.268 & \mu_{12} &= 0.266 & \mu_{13} &= 0.277 & \mu_{14} &= 0.230 \\
 \mu_{21} &= 0.093 & \mu_{22} &= 0.112 & \mu_{23} &= 0.227 & \mu_{24} &= 0.188 \\
 \mu_{31} &= 0.046 & \mu_{32} &= 0.018 & \mu_{33} &= 0.170 & \mu_{34} &= 0.078 \\
 \mu_{41} &= 0.041 & \mu_{42} &= 0.065 & \mu_{43} &= 0.178 & \mu_{44} &= 0.095
 \end{aligned}$$

Although these values are specific to our hardware, they show the significance of these biases given the current

operating scale as well as how much variation there is between pairs of sensors (i.e., as much as 25.9 cm between our observed best and worst pair).

C. Trials

Several experiments were run with different trajectories and durations. In all trials the Turtlebots were driven at the maximum velocity and rotation rate (1 m/s of 1 rad/s respectively). The specific trials were:

- rot-cw/rot-ccw: R_A is kept stationary. R_B is placed a fixed distance away and rotated clockwise/counter-clockwise in place.
- traj-cw/traj-ccw: R_A is kept stationary. R_B is manually driven in a circular trajectory about R_A in a clockwise/counter-clockwise direction.
- kidney-bean: R_A is kept stationary. R_B is manually driven in a kidney bean shape while pausing briefly throughout the trajectory (See Figure 6).
- box: R_A is kept stationary. R_B is manually driven in an approximately 8 m by 6 m rectangle.
- both-move: Both R_A and R_B are manually driven arbitrarily within within a 10 m by 10 m space without getting within 1 m of each other.

All results are compiled into Tables II and III, showing the mean, max, and standard deviation of the position and absolute heading errors respectively.

D. Interpreting Results

The results in Tables II and III show that Weighted and Unweighted consistently outperform the other approaches; this makes clear the advantage of the calibrated $\hat{z}_{ij}^{(t)}$ over the raw $z_{ij}^{(t)}$ or the individual mean shift/moving average corrections. Additionally, Weighted consistently outperforms Unweighted in mean positional error. Next,

TABLE II: Evaluation of positional error in meters between algorithms and datasets.

Position Error [m]	Scenario																				
	rot-cw			rot-ccw			traj-cw			traj-ccw			kidney-bean			box			both-move		
Method	Mean	Max	Std	Mean	Max	Std	Mean	Max	Std	Mean	Max	Std	Mean	Max	Std	Mean	Max	Std	Mean	Max	Std
Raw	0.44	0.98	0.16	0.38	0.65	0.08	0.98	5.71	0.88	0.59	1.54	0.30	0.76	5.20	0.68	0.93	4.99	0.70	0.82	3.50	0.54
Shift only	0.27	0.72	0.15	0.19	0.46	0.09	0.70	5.27	0.89	0.27	1.27	0.25	0.47	4.77	0.73	0.44	4.61	0.69	0.42	3.53	0.48
MovingAvg only	0.35	0.53	0.05	0.34	0.47	0.05	0.87	5.08	0.65	0.55	1.41	0.27	0.68	3.40	0.47	0.91	3.57	0.59	0.78	2.64	0.42
Unweighted (Eq. 3)	0.14	0.25	0.02	0.13	0.19	0.02	0.62	4.37	0.70	0.22	1.02	0.19	0.36	2.91	0.44	0.45	3.29	0.54	0.37	2.87	0.42
Weighted (Eq. 8) [Proposed]	0.09	0.21	0.06	0.09	0.21	0.05	0.20	1.41	0.18	0.21	0.86	0.16	0.13	0.52	0.11	0.21	0.96	0.17	0.29	2.70	0.32

TABLE III: Evaluation of absolute heading error in degrees between algorithms and datasets.

Abs Heading Error [deg]	Scenario																				
	rot-cw			rot-ccw			traj-cw			traj-ccw			kidney-bean			box			both-move		
Method	Mean	Max	Std	Mean	Max	Std	Mean	Max	Std	Mean	Max	Std	Mean	Max	Std	Mean	Max	Std	Mean	Max	Std
Raw	9.82	21.81	5.53	10.10	22.43	6.05	16.82	90.29	15.09	12.44	35.78	9.38	12.06	70.33	12.17	12.11	65.86	10.15	11.35	72.69	9.33
Shift only	6.38	16.44	4.19	6.45	14.20	4.09	12.40	90.41	15.52	6.99	31.55	6.44	8.10	80.20	12.72	6.34	64.33	9.76	6.97	78.23	9.46
MovingAvg only	7.05	14.70	4.63	7.37	17.59	4.68	14.48	77.47	11.49	11.27	35.41	8.70	10.32	57.96	8.73	11.55	50.65	9.01	11.11	55.54	7.15
Unweighted (Eq. 3)	3.31	8.28	1.99	2.88	9.78	2.13	10.77	72.66	11.65	5.44	25.92	4.79	6.15	58.70	8.38	5.99	51.71	7.91	6.38	53.30	7.64
Weighted (Eq. 8) [Proposed]	4.12	10.78	3.11	4.43	10.53	3.34	5.88	75.56	8.09	5.84	31.01	6.05	3.95	11.97	2.98	4.22	13.31	3.03	5.45	104.00	9.97

while Unweighted outperforms Weighted in a few select metrics in the simpler rot-* and traj-* trials, this is only by relatively small margins (i.e., at most 4 cm or 5.1 deg respectively). When considering the more challenging kidney-bean and box trajectories, we see Weighted substantially outperforms Unweighted in all metrics. Finally, when examining both-move, we see Weighted outperforms all other methods in the three positional error metrics as well as mean absolute heading error. The spike observed in Weighted’s other two heading metrics appears to be the result of rapid relative yawing, possible when R_A and R_B yaw simultaneously at max speed in opposite directions.

E. Comparison to Literature

Our box trial was designed so that it can be compared to a similar experiment in [19]. Note that both experiments used two Turtlebots (one stationary, one moving), each equipped with four Nooploop LinkTrack P UWB modules separated by an approximately 70 cm baseline, and performed relative pose estimation while traversing an approximately 8 m by 6 m rectangle. When comparing our results to the reported results in [19], our proposed approach, Weighted, achieved slightly better position error (0.21 m vs 0.25 m), but with slightly worse mean heading error (4.22 deg vs 2.02 deg) and standard deviations (our 0.17 m and 3.03 deg vs their 0.09 m 1.47 deg respectively). Thus, our approach is competitive with the performance in [19], but that work assumes access to **continuously transmitted odometry estimates, whereas our approach does not.**

VI. CONCLUSION

We proposed a multi-agent 2D relative pose localization approach that does not rely on any external infrastructure or data exchange between agents, just multiple locally collected UWB range measurements. By integrating a priori knowledge about our observed measurement biases and obstruction patterns, we achieve competitive results with works such as [19], but without needing continuously transmitted odometry between agents.

In the future, we plan to extend this approach to 3D pose, while maintaining minimalist communication requirements. We will also investigate increasing the team to have more

agents, better modeling of the range measurement noise, estimating our pose covariance through more powerful optimization libraries, and taking a more rigorous approach to our observability analysis. Finally, we will directly integrate this system into full-scale multi-agent collaborative SLAM pipeline, like Kimera-Multi [5].

REFERENCES

- [1] Yulun Tian, Katherine Liu, Kyel Ok, Loc Tran, Danette Allen, Nicholas Roy, and Jonathan P. How. Search and rescue under the forest canopy using multiple uavs. *Int. J. Robotics Res.*, 39(10-11), 2020.
- [2] Xiulong Liu, Jiannong Cao, Yanni Yang, and Shan Jiang. Cps-based smart warehouse for industry 4.0: A survey of the underlying technologies. *Comput.*, 7(1):13, 2018.
- [3] Ali Agha, Kyohei Otsu, Benjamin Morrell, David D. Fan, Rohan Thakker, and et al. Nebula: Quest for robotic autonomy in challenging environments; TEAM costar at the DARPA subterranean challenge. *CoRR*, abs/2103.11470, 2021.
- [4] Xun S. Zhou and Stergios I. Roumeliotis. Robot-to-robot relative pose estimation from range measurements. *IEEE Trans. Robotics*, 24(6):1379–1393, 2008.
- [5] Yun Chang, Yulun Tian, Jonathan P. How, and Luca Carlone. Kimera-multi: a system for distributed multi-robot metric-semantic simultaneous localization and mapping. In *IEEE International Conference on Robotics and Automation, ICRA 2021, Xi’an, China, May 30 - June 5, 2021*, pages 11210–11218. IEEE, 2021.
- [6] Pierre-Yves Lajoie, Benjamin Ramtoula, Yun Chang, Luca Carlone, and Giovanni Beltrame. DOOR-SLAM: distributed, online, and outlier resilient SLAM for robotic teams. *IEEE Robotics Autom. Lett.*, 5(2):1656–1663, 2020.
- [7] Titus Cieslewski, Siddharth Choudhary, and Davide Scaramuzza. Data-efficient decentralized visual SLAM. In *2018 IEEE International Conference on Robotics and Automation, ICRA 2018, Brisbane, Australia, May 21-25, 2018*, pages 2466–2473. IEEE, 2018.
- [8] Xinya Li, Zhiqun Daniel Deng, Lynn T Rauchenstein, and Thomas J Carlson. Contributed review: Source-localization algorithms and applications using time of arrival and time difference of arrival measurements. *Review of Scientific Instruments*, 87(4):041502, 2016.
- [9] Erin Marie Fischell, Nicholas Rahardiyan Rypkema, and Henrik R. Schmidt. Relative autonomy and navigation for command and control of low-cost autonomous underwater vehicles. *IEEE Robotics Autom. Lett.*, 4(2):1800–1806, 2019.
- [10] Kang Eun Jeon, James She, Perm Soonsawad, and Pai Chet Ng. BLE beacons for internet of things applications: Survey, challenges, and opportunities. *IEEE Internet Things J.*, 5(2):811–828, 2018.
- [11] Taweesak Sanpechuda and La-or Kovavisaruch. A review of rfid localization: Applications and techniques. In *2008 5th international conference on electrical engineering/electronics, computer, telecommunications and information technology*, volume 2, pages 769–772. IEEE, 2008.

- [12] Fernando Herranz, Angel Llamazares, Eduardo J. Molinos, and Manuel Ocaña. A comparison of SLAM algorithms with range only sensors. In *IEEE International Conference on Robotics and Automation, ICRA*, pages 4606–4611. IEEE, 2014.
- [13] Aditya Arun, Roshan Ayyalasomayajula, William Hunter, and Dinesh Bharadia. P2slam: Bearing based wifi slam for indoor robots. *IEEE Robotics and Automation Letters*, 2022.
- [14] Abdulrahman Alarifi, AbdulMalik S. Al-Salman, Mansour Alsaleh, Ahmad Alnafessah, Suheer Alhadhrami, Mai A. Al-Ammar, and Hend S. Al-Khalifa. Ultra wideband indoor positioning technologies: Analysis and recent advances. *Sensors*, 16(5):707, 2016.
- [15] Nour Smaoui, Omprakash Gnawali, and Kyungki Kim. Study and mitigation of platform related UWB ranging errors. In *2020 International Conference on Communication Systems & NETWORKS, COMSNETS 2020, Bengaluru, India, January 7-11, 2020*, pages 346–353. IEEE, 2020.
- [16] Anton Ledergerber and Raffaello D’Andrea. Ultra-wideband range measurement model with gaussian processes. In *IEEE Conference on Control Technology and Applications, CCTA 2017, Mauna Lani Resort, HI, USA, August 27-30, 2017*, pages 1929–1934. IEEE, 2017.
- [17] Anton Ledergerber and Raffaello D’Andrea. Calibrating away inaccuracies in ultra wideband range measurements: A maximum likelihood approach. *IEEE Access*, 6:78719–78730, 2018.
- [18] Michael Hamer and Raffaello D’Andrea. Self-calibrating ultra-wideband network supporting multi-robot localization. *IEEE Access*, 6:22292–22304, 2018.
- [19] Zhiqiang Cao, Ran Liu, Chau Yuen, Achala Athukorala, Benny Kai Kiat Ng, Muraleetharan Mathanraj, and U-Xuan Tan. Relative localization of mobile robots with multiple ultra-wideband ranging measurements. In *IEEE/RSJ International Conference on Intelligent Robots and Systems, IROS 2021, Prague, Czech Republic, September 27 - Oct. 1, 2021*, pages 5857–5863. IEEE, 2021.
- [20] Hao Xu, Luqi Wang, Yichen Zhang, Kejie Qiu, and Shaojie Shen. Decentralized visual-inertial-uwb fusion for relative state estimation of aerial swarm. In *2020 IEEE International Conference on Robotics and Automation, ICRA 2020, Paris, France, May 31 - August 31, 2020*, pages 8776–8782. IEEE, 2020.
- [21] Hao Xu, Yichen Zhang, Boyu Zhou, Luqi Wang, Xinjie Yao, Guotao Meng, and Shaojie Shen. Omni-swarm: A decentralized omnidirectional visual-inertial-uwb state estimation system for aerial swarm. *CoRR*, abs/2103.04131, 2021.
- [22] Yulun Tian, Kasra Khosoussi, and Jonathan P. How. A resource-aware approach to collaborative loop-closure detection with provable performance guarantees. *Int. J. Robotics Res.*, 40(10-11), 2021.
- [23] Xianjia Yu, Qingqing Li, Jorge Peña Queralta, Jukka Heikkonen, and Tomi Westerlund. Applications of UWB networks and positioning to autonomous robots and industrial systems. In *10th Mediterranean Conference on Embedded Computing, MECO 2021, Budva, Montenegro, June 7-10, 2021*, pages 1–6. IEEE, 2021.
- [24] Michael Strohmeier, Thomas Walter, Julian Rothe, and Sergio Montenegro. Ultra-wideband based pose estimation for small unmanned aerial vehicles. *IEEE Access*, 6:57526–57535, 2018.
- [25] Bo Yang, Jun Li, and Hong Zhang. Uvip: Robust uwb aided visual-inertial positioning system for complex indoor environments. In *2021 IEEE International Conference on Robotics and Automation (ICRA)*, pages 5454–5460. IEEE, 2021.
- [26] Daniele Fontanelli, Farhad Shamsfakhr, Paolo Bevilacqua, and Luigi Palopoli. UWB indoor global localisation for nonholonomic robots with unknown offset compensation. In *IEEE International Conference on Robotics and Automation, ICRA 2021, Xi’an, China, May 30 - June 5, 2021*, pages 5795–5801. IEEE, 2021.
- [27] Thien Hoang Nguyen, Thien-Minh Nguyen, and Lihua Xie. Range-focused fusion of camera-imu-uwb for accurate and drift-reduced localization. *IEEE Robotics Autom. Lett.*, 6(2):1678–1685, 2021.
- [28] Mark W. Müller, Michael Hamer, and Raffaello D’Andrea. Fusing ultra-wideband range measurements with accelerometers and rate gyroscopes for quadcopter state estimation. In *IEEE International Conference on Robotics and Automation, ICRA 2015, Seattle, WA, USA, 26-30 May, 2015*, pages 1730–1736. IEEE, 2015.
- [29] Saman Fahandezh-Saadi and Mark W. Mueller. Optimal measurement selection algorithm and estimator for ultra-wideband symmetric ranging localization. *CoRR*, abs/1804.09773, 2018.
- [30] Sungjae Shin, Eungchang Mason Lee, Junho Choi, and Hyun Myung. MIR-VIO: mutual information residual-based visual inertial odometry with UWB fusion for robust localization. *CoRR*, abs/2109.00747, 2021.
- [31] Nobuhiro Funabiki, Benjamin Morrell, Jeremy Nash, and Ali-akbar Agha-mohammadi. Range-aided pose-graph-based SLAM: applications of deployable ranging beacons for unknown environment exploration. *IEEE Robotics Autom. Lett.*, 6(1):48–55, 2021.
- [32] Mohammed Shalaby, Charles Champagne Cossette, James Richard Forbes, and Jerome Le Ny. Relative position estimation in multi-agent systems using attitude-coupled range measurements. *IEEE Robotics Autom. Lett.*, 6(3):4955–4961, 2021.
- [33] Charles Champagne Cossette, Mohammed Shalaby, David Saussié, James Richard Forbes, and Jerome Le Ny. Relative position estimation between two UWB devices with imus. *IEEE Robotics Autom. Lett.*, 6(3):4313–4320, 2021.
- [34] Chiara Bonsignori, Fabio Condomitti, Marco Del Gamba, Federico Garzelli, Leonardo Lossi, Francesco Mione, Alessandro Noferi, and Alessio Vecchio. Estimation of user’s orientation via wearable UWB. In *16th International Conference on Intelligent Environments, IE 2020, Madrid, Spain, July 20-23, 2020*, pages 80–83. IEEE, 2020.
- [35] Ehab Ghanem, Kyle O’Keefe, and Richard Klukas. Testing vehicle-to-vehicle relative position and attitude estimation using multiple UWB ranging. In *92nd IEEE Vehicular Technology Conference, VTC Fall 2020, Victoria, BC, Canada, November 18 - December 16, 2020*, pages 1–5. IEEE, 2020.
- [36] Ernst-Johann Theussl, Dimitar Ninevski, and Paul O’Leary. Measurement of relative position and orientation using UWB. In *IEEE International Instrumentation and Measurement Technology Conference, I2MTC 2019, Auckland, New Zealand, May 20-23, 2019*, pages 1–6. IEEE, 2019.
- [37] Thien-Minh Nguyen, Abdul Hanif Bin Zaini, Chen Wang, Kexin Guo, and Lihua Xie. Robust target-relative localization with ultra-wideband ranging and communication. In *2018 IEEE International Conference on Robotics and Automation, ICRA 2018, Brisbane, Australia, May 21-25, 2018*, pages 2312–2319. IEEE, 2018.
- [38] Tong Qin, Peiliang Li, and Shaojie Shen. Vins-mono: A robust and versatile monocular visual-inertial state estimator. *IEEE Trans. Robotics*, 34(4):1004–1020, 2018.
- [39] Christoph Steup, Jonathan Beckhaus, and Sanaz Mostaghim. A single-copter uwb-ranging-based localization system extendable to a swarm of drones. *Drones*, 5(3):85, 2021.
- [40] Nooploop. *LinkTrack User Manual*, v2.1 edition.
- [41] Nooploop. *LinkTrack Datasheet*, v2.1 edition.
- [42] Pauli Virtanen, Ralf Gommers, Travis E. Oliphant, Matt Haberland, Tyler Reddy, et al., and SciPy 1.0 Contributors. SciPy 1.0: Fundamental Algorithms for Scientific Computing in Python. *Nature Methods*, 17:261–272, 2020.
- [43] Ralph B d’Agostino. An omnibus test of normality for moderate and large size samples. *Biometrika*, 58(2):341–348, 1971.
- [44] Morgan Quigley, Ken Conley, Brian Gerkey, Josh Faust, Tully Foote, Jeremy Leibs, Rob Wheeler, Andrew Y Ng, et al. Ros: an open-source robot operating system. In *ICRA workshop on open source software*, volume 3, page 5. Kobe, Japan, 2009.